GT2021-59334

A DETAILED LOSS ANALYSIS METHODOLOGY FOR CENTRIFUGAL COMPRESSORS

Luying Zhang¹, Loukia Kritioti¹, Peng Wang¹, Jiangnan Zhang¹, Mehrdad Zangeneh²

¹Advanced Design Technology, 30 Millbank, Westminster, London, SW1P 4DU, UK ²Department of Mechanical Engineering, University College London, Torrington Place, London, WC1E 7JE, UK

ABSTRACT

A deep understanding of loss mechanisms inside a turbomachine is crucial for the design and analysis work. By quantifying the various losses generated from different flow mechanisms, a targeted optimization can be carried out on the blading design. To meet the ever-growing requirements on high efficiency and wide operational range, an effective detailed loss analysis is required by the designers. In this paper an evaluation method for computational fluid dynamics simulations has been developed to quantify the loss generation based on entropy production in the flow field. A breakdown of losses caused by different mechanisms (such as skin friction, secondary flow, tip clearance vortex and shock waves) is achieved by separating the flow field into different zones. Each zone is defined by the flow physics rather than by geometrical locations or empirical correlations, which makes the method a more general approach and applicable to different machine types.

The method has been applied to both subsonic and transonic centrifugal compressors, where internal flow is complex due to the Coriolis acceleration and the curvature effect. An evaluation of loss decomposition is obtained at various operational conditions. The impact of design modification is also assessed by applying the same analysis to an optimized design.

Keywords: loss generation, entropy production, centrifugal compressors, design optimization.

NOMENCLATURE

Place nomenclature section, if needed, here. Nomenclature should be given in a column, like this:

α	alpha
β	beta
γ	gamma
δ	delta
3	epsilon, etc.

1. INTRODUCTION

aerodynamic performance To achieve good turbomachines an evaluation on loss generation inside a blade row is essential. Empirical loss correlations calibrated by experimental data have been developed in the past and have become the backbone of the design system. A highly accurate loss prediction is important in the initial design phase. On the other hand, during the design iterations and optimization work, a detailed loss analysis is needed to gain better understanding of the complex 3D flow field inside a blade row. The development of Computational Fluid Dynamics (CFD) enables the feedbacks from numerical simulations with the resolution based on mesh elements. Yet, a loss evaluation methodology needs to be developed, if loss contributions from different mechanisms or related to different design features are to be quantified. Such information will greatly help the designers understand the loss generation and identify the key areas to be improved. In addition, the ever-growing requirement on efficiency, the demand on operational flexibility, cost reduction and new manufacturing techniques all put challenges on the aerodynamic design. To meet these challenging requirements and to further optimize the performance a systematic loss analysis method is valuable.

In the previous studies, it was deduced that loss generation can be measured by entropy production in an adiabatic machine [1]. The isentropic efficiency is reduced by irreversible flow processes such as viscous dissipation and heat transfer or nonequilibrium processes (shock wave, condensation, cavitation etc.), which all create entropy. The rate of entropy generation per volume gives a quantitative accounting of the local entropy production in the flow field [2]. It is made particularly advantageous by CFD simulations where entropy generation rate in mesh element level can be extracted from the flow solutions. The local entropy production gives the designer insight into the

performance of a machine and helps identify high loss regions in a design.

Meanwhile, in order to obtain local entropy generation rate in turbulent flow, some modeling is needed on small scale eddies without applying Direct Numerical Simulation (DNS). Such simulations are time-consuming and not practical during daily design iterations. Previous study by Moore and Moore [2] used the eddy viscosity to model the turbulent viscous dissipation and temperature fluctuation dissipation. Kock and Herwig [3] also investigated the entropy production in turbulence shear flow. The Reynolds-averaging procedure was extended to the entropy balance equation. They proposed models for the Reynolds-Averaged Navier-Stokes (RANS) simulation to calculate entropy generation rate and developed wall functions for entropy production terms to better represent near wall regions. Jin et al. [4] proposed similar concepts to Moore and Moore's work for calculating the entropy production rate with RANS simulations based on eddy viscosity hypothesis. More recently, Zhao and Sandberg [5] compared the entropy generation terms produced by a large-eddy simulation (LES) and by RANS in a 2D highpressure turbine vane passage. The biggest difference of the turbulence production term was found in the wake region.

With the local entropy generation rate per unit volume obtained from the CFD solution, a 'loss audit' in different areas of a blade row is possible. Pullan et al. [6] applied the analysis to a low aspect ratio turbine nozzle guide vane and highlighted the areas where the loss reduction has occurred when employing highly aft-loaded design. Newton et al. [7] conducted the aerodynamic loss audit in a double entry turbocharger turbine under full admission and partial admission conditions. The distribution of loss within the turbine is evaluated and compared for each condition. The loss distribution in the partial admission case was found to be very different to that seen in the full admission case. Denton and Pullan [8] studied the end-wall loss in a large-scale low-speed turbine cascade using a loss breakdown obtained by integrating the entropy production rate. The passage flow was divided into different regions and the loss generated in each region was computed by integration over the volume. Yoon et al. [9] also tried to carry out a loss audit in an axial turbine stage. Rather than separating the fluid domain into different regions, they performed a set of 'numerical experiments' by turning off the viscosity on the endwall or on the airfoil. When comparing to the datum case (including all the viscous effects and leakage flow), the reduction of aerodynamic loss was used to indicate the loss contribution from each source.

The breakdown of loss generation is a rather sophisticated subject. The aforementioned studies either divided the fluid domain by geometrical locations or turned off certain loss sources through numerical experiments. In an actual 3D flow field, the streamwise vorticity will develop whenever a moving fluid with a gradient of the reduced static pressure turns around a bend or rotates about an axis [10]. The gradients of the reduced static pressure are produced as a result of nonuniform velocity profile, centrifugal force and Coriolis force [11] [12], which are inevitable in a turbomachine. The streamwise vorticity will encourage the secondary flow inside a passage and a passage

vortex can develop within the blade row. The interaction between the secondary flow and the boundary layer flow together with the viscous dissipation in the passage vortex create significant contribution to the loss generation. For an axial turbine the endwall loss typically accounts for about 1/3 of the total loss [1]. The streamwise vortices also creates complex 3D flow patterns inside a blade row, which cannot be depicted by simple geometrical domain separation. For unshrouded blade rows, the tip leakage flow also forms vortex and further complicate the flow structure. These are especially important for centrifugal machines where the effective aspect ratio is usually low compared to axial machines. The passage vortex and tip clearance vortex can impact a big portion of the blade span towards the trailing edge. A simple breakdown of the fluid domain by spanwise or pitchwise position cannot capture the zones impacted by the vortices with good accuracy. A breakdown methodology based on flow physics is needed instead.

Grübel et al. [13] developed a methodology for detailed loss prediction in low pressure steam turbines. The entropy flux through the cell faces was calculated instead of using the rate of entropy generation per volume to get the local entropy generation. However, some programing work had to be done to restructure the mesh as an unstructured solver was used in the numerical simulations. The loss analysis was carried out on a 2D streamtube extracted from the 3D CFD solution. The streamtube was separated into different categories using the physical features of the different loss mechanisms. For example, the boundary layer region was identified by finding the location where the velocity tangential to the wall reaches 99% of the free stream velocity. The shock region was identified with the help of a limiting value of the projection of the density gradient on the normalized velocity vector. By setting up appropriate limiting criteria they could separate the boundary layer loss, wake mixing loss and shock loss in the streamtube. In addition, the nonequilibrium thermodynamic relaxation loss caused by condensation in a low-pressure steam turbine can be computed using the entropy production rate associated with the release of latent heat between droplet and vapor temperature. So, the loss due to the irreversible phase change in the flow field can be taken into account. Sun [14] established the entropy production equations for cavitation flow. When cavitation occurs the energy exchange involves latent heat of phase change. The entropy production due to cavitation was modeled and quantified. The method was demonstrated on a NACA hydrofoil and a 3D propeller. Recently, Saito et al. [15] evaluated the flow loss generation in a transonic axial compressor using a large scale detached eddy simulation (DES). They used vortex identification and flow visualization techniques to break down the loss generation into different categories: boundary layer, wake, shock wave, hub-corner separation and tip leakage vortex. The condition for dividing those regions was defined by the vorticity, normalized helicity, entropy, total pressure and static pressure. The loss decomposition for the rotor and stator blade row was obtained for operating point at design rotational speed and at 50% design rotational speed.

These previous studies were mainly carried out for axial machines. No systematic loss breakdown has been carried out for centrifugal machine using entropy generation analysis and with physics-based flow structure identification criteria. In this paper, a detailed loss analysis method has been developed for centrifugal compressors. The loss generation is calculated from the rate of entropy generation in turbulent flow. A breakdown of losses caused by different mechanisms (shock waves, skin friction, secondary flow and tip clearance vortex) is achieved by separating the flow field into different zones. The separation is defined by the physical parameters rather than by geometrical locations or empirical correlations. The method has been applied to a subsonic and a transonic centrifugal compressor, where the internal flow is complex and the secondary flow is strong due to Coriolis acceleration and the meridional curvature effect. The evaluation of loss generation is done for both design condition and off-design conditions. It is also conducted on optimized designs to show the impact of design modifications.

2. OUTLINE OF THE PAPER

The layout of the paper is as follows. The entropy generation rate which is used to calculate the local loss production is discussed first for turbulent flow. The equations are formed for RANS simulations, which are employed for the CFD studies in this work. Secondly the loss breakdown criteria for each category including shock waves, skin friction, secondary flow and tip clearance vortex are described in detail. The next section introduces the CFD setup and validation. The simulation results for both the subsonic compressor and transonic compressor are compared to test data. A mesh sensitivity study has been carried out with an emphasis on the prediction for entropy generation. Then the detailed loss analysis on both machines is conducted and, in both cases, an optimized design through 3D inverse design method [16] [17] has been analyzed for comparison. Finally, conclusions are drawn on the results and further discussion on how to extend/improve the method is provided.

3. LOSS ANALYSIS METHODOLOGY

The entropy equation can be deduced from the conservation of momentum and energy equation combined with the fundamental thermodynamic equation:

$$\dot{S}_{vol} = \frac{1}{T} \tau_{ij} \frac{\partial u_i}{\partial x_j} + \frac{k}{T^2} \left(\frac{\partial T}{\partial x_j} \right)^2 \tag{1}$$

 \dot{S}_{vol} is the entropy generation rate per volume. It has the unit of Watt/(m³K). k is thermal conductivity. It is assumed that the system is adiabatic and there is no heat source such as a combustion or a radiation. The first term on the right-hand side is due to viscous effect. The second term is the contribution from heat flux. Fourier's law is assumed for the heat conduction. When applying Reynolds averaging to the system, the two terms can be decomposed into the mean flow and fluctuation part [3]:

$$\dot{S}_{vol} = \dot{S}_{vol,\bar{D}} + \dot{S}_{vol,D'} + \dot{S}_{vol,\bar{C}} + \dot{S}_{vol,C'}$$
 (2)

$$\dot{S}_{vol,\bar{D}} = \frac{1}{\bar{\tau}} \bar{\tau}_{ij} \frac{\partial \bar{u}_i}{\partial x_i} \tag{3}$$

$$\dot{S}_{vol,D'} = \frac{1}{\bar{\tau}} \overline{\tau'_{iJ} \frac{\partial u'_{i}}{\partial x_{J}}} \tag{4}$$

$$\dot{S}_{vol,\bar{C}} = \frac{k}{\bar{T}^2} \left(\frac{\partial \bar{T}}{\partial x_j} \right)^2 \tag{5}$$

$$\dot{S}_{vol,C'} = \frac{k}{\bar{T}^2} \left(\frac{\partial T'}{\partial x_1} \right)^2 \tag{6}$$

 $\dot{S}_{vol,\bar{D}}$ and $\dot{S}_{vol,\bar{C}}$ can be calculated directly from the mean flow variables. $\dot{S}_{vol,D'}$ and $\dot{S}_{vol,C'}$ contain the turbulent fluctuation terms, which cannot be calculated directly from RANS solutions. Using eddy viscosity to model the turbulent viscous dissipation and assuming the effect of turbulence on heat transfer can be approximated in a similar way [2], the fluctuation terms can be expressed as:

$$\dot{S}_{vol,D'} \cong \frac{\mu_t}{\mu} \frac{1}{\bar{\tau}} \bar{\tau}_{ij} \frac{\partial \bar{u}_i}{\partial x_i} \tag{7}$$

$$\dot{S}_{vol,C'} \cong \frac{k_t}{\bar{T}^2} \left(\frac{\partial \bar{T}}{\partial x_i} \right)^2 \tag{8}$$

$$k_t = \frac{c_p \mu_t}{Pr_t} \tag{9}$$

Turbulent Prandtl number Pr_t is assumed to be 1. With these approximation, all four terms can be calculated with RANS solution under eddy viscosity hypothesis. In an adiabatic system without significant temperature variation the entropy generation terms associated with heat flux are generally much smaller than those from viscous dissipation.

Once the entropy generation rate per volume has been computed from the CFD solutions, the local entropy production information will be available from each mesh element. The integration over a certain volume will give the entropy production rate in that region. The next step is to divide the computational domain into different regions that account for different mechanism of loss generation.

3.1 Shock Losses

To identify the zones where shock waves are formed, the projection of the density gradient on the normalized velocity vector is calculated [13]:

$$\varepsilon = \nabla \rho \cdot \frac{c}{|c|} \tag{10}$$

 ε < 0 represents an expansion and ε > 0 represents a compression. By setting up a limiting value of ε the non-isentropic compression waves can be filtered out from the flow field. Elements that satisfy this criterion will be attributed to 'shock zone'. The volume integration of the entropy generation rate will give the entropy created by shock waves and therefore the losses produced.

3.2 Boundary Layer Losses

Within the boundary layer, the rate of entropy generation per unit volume (due to viscous effects) can be simplified using scale analysis [1] to the expression given in equation 11:

$$\dot{S}_{vol,D} = \frac{1}{T} \tau \frac{dV}{dv} \tag{11}$$

Where y is the direction perpendicular to the boundary layer stream tube. For most boundary layers, the flow velocity changes rapidly near the wall surface, hence most of the entropy generation is concentrated in the inner part of the boundary layer. For turbulent boundary layers, the near wall velocity gradient is steep and consequently the entropy production rate has a high value near the wall.

Dawes [18] studied the breakdown of the entropy generation in a turbulent boundary layer. The results showed 50% of the loss is generated between the wall and the edge of the sublayer at $y + \sim 10$ and 90% of the loss is generated between the wall and the edge of the logarithmic zone at $y + \sim 30$.

This high entropy production rate region in the boundary layer can be identified by the high turbulence eddy dissipation near the wall surface. An experimental study conducted at a Reynolds number (based on boundary layer thickness) of 4230 shows that turbulence kinetic energy dissipation rate grows rapidly where y + is below 30 [19].

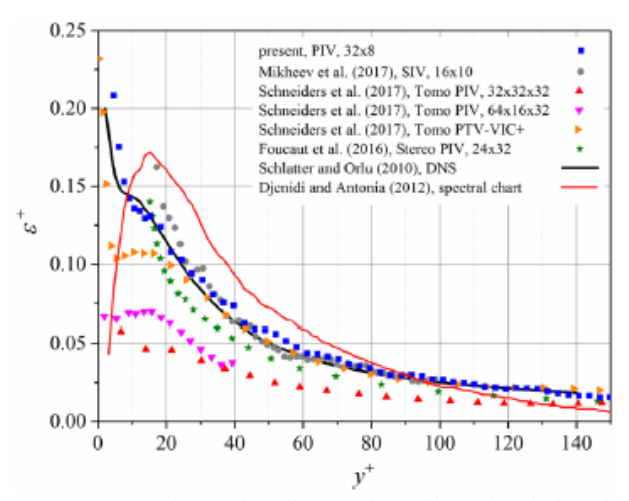


Figure 1. Comparison of wall-normal profiles of turbulent kinetic energy dissipation rate estimated by different techniques (Zaripov et al. [19])

3.3 Secondary Flow Losses

The secondary flow loss is difficult to predict well by empirical correlations. 3D numerical simulations provide better accuracy in capturing the main flow structure inside a blade row. This is particularly important to centrifugal compressors, where flow within the impeller is always highly three dimensional. As described by Zangeneh [17], the axial to radial bend induces strong secondary flow, transporting low momentum fluid from hub to shroud on both the suction and pressure surface of the blade. Pressure to suction surface secondary flow in the end wall is also triggered by the tangential component of Coriolis acceleration. In the purely radial part of the impeller strong blade to blade secondary flow is formed. As a result, the high-entropy, low momentum fluid concentrates at the suction surface near the shroud, which forms the well-known jet-wake structure at the exit of the impeller.

The first measurements using laser anemometry by Eckardt [20] [21] provided important information on the flow structures inside centrifugal compressor impellers. Eckardt showed that the secondary flow pattern can be extracted from the measured velocity field inside the passage. The measurements in Eckardt's work also provided a high-quality data set for numerical method verification. Previous studies [22][23] showed that the flow structures measured by Eckardt can be captured well by 3D viscous CFD simulations.

Since the secondary flow is caused by the vorticity in the flow field and evolves into a secondary flow vortex in the passage, it is rational to use vortex identification techniques to separate the secondary flow from the mainstream flow. The Q-Criterion (the second invariant of the velocity gradient tensor) is used in this work to identify the vortex zone in the passage flow.

The velocity gradient tensor $D_{ij} = \frac{\partial u_i}{\partial x_j}$ can be decomposed

into a symmetric and a skew-symmetric part:

$$D_{ij} = S_{ij} + \Omega_{ij} \tag{12}$$

Where
$$S_{ij} = \frac{1}{2} \left(\frac{\partial u_i}{\partial x_j} + \frac{\partial u_j}{\partial x_i} \right)$$
 and $\Omega_{ij} = \frac{1}{2} \left(\frac{\partial u_i}{\partial x_j} - \frac{\partial u_j}{\partial x_i} \right)$. S_{ij} is the

rate-of-strain tensor and Ω_{ij} is the vorticity tensor.

The characteristic equation for ∇u is written as:

$$\lambda^3 + P\lambda^2 + Q\lambda + R = 0 \tag{13}$$

Where P, Q and R are the three invariants of the velocity gradient tensor.

The Q-criterion is derived based on the second invariant Q in Equation 13. Using the decomposition, it can be expressed as:

$$Q = \frac{1}{2} (\|\Omega\|^2 - \|S\|^2)$$
 (14)

The Q-criterion defines vortices as the area where the vorticity magnitude is greater than the magnitude of the rate of strain. Q > 0 represents the existence of a vortex. The value of Q can be used to visualize and separate vortex structures in the flow field.

3.4 Tip Leakage Losses

In unshrouded compressor the pressure difference between pressure side and suction side will drive flow over the blade tip and form a tip leakage vortex. In the potential theory the flow around an airfoil can be obtained from a potential vortex superposed on a parallel flow. According to Helmholtz's vortex law, a vortex line in inviscid flows cannot end at the blade tip. A vortex filament is shed from the blade tip in the main flow direction. The vorticity of the blade tip vortex can be linked to the blade force and therefore the blade loading through Kutta-Joukowski theorem and Stokes' theorem. In actual flow field viscous effect will take place in the vortex and the mixing of leakage vortex flow and the mainstream flow also create aerodynamic loss.

The interaction between the leakage flow and the secondary flow can be strong in the rear part of the impeller suction surface. The 'wake' flow will mix with the fluid flowing over the blade tip. Therefore, the two vortices are difficult to separate. In fact, some methods do not distinguish the leakage loss from the secondary flow loss.

In this work the two was separated by the turbulence kinetic energy and by the absolute helicity. Helicity is defined as the dot product of velocity vector and vorticity vector.

$$H = (\nabla \times \boldsymbol{u}) \cdot \boldsymbol{u} \tag{15}$$

The tip leakage vortex filament is roughly in the main flow direction and tends to have higher absolute helicity compared to the secondary flow vortex. The turbulence kinetic energy within the tip leakage vortex also tends to be higher than the passage vortex [25]. Combining these two criteria and with the help of flow visualization the tip leakage vortex zone can be separated from the fluid domain.

Using the aforementioned criteria, it is possible to divide the impeller passage into different zones. To avoid overlapping and losses in some region being counted more than once, each zone will exclude the mesh elements that fit into other criteria. The division was conducted in order of the shock wave, the boundary layer, the secondary flow and tip leakage flow.

4. NUMERICAL SETUP AND VALIDATION

The methodology will be demonstrated in two centrifugal compressors. A validation of the numerical method was conducted first by comparing the CFD results to the test data available for the two compressors.

The first example is the widely known Eckardt's impeller "A" [21]. The first laser measurements by Eckardt were carried out on a radial centrifugal compressor, which was known as Eckardt's impeller "0". The same shroud shape was used for impeller "A". The blade shape from inducer to 80 percent of the outlet radius is also the same as impeller "0". Towards the trailing edge the blade was modified to have 30-degrees backsweep and the hub contour was moved outwards. The key geometrical information is listed in Table 1.

Table 1. Geometry of the Eckardt "A" impeller.

Number of blades Z	20
Impeller diameter D2	400 [mm]
Impeller outlet width b2	26 [mm]
Inlet shroud radius r1s	140[mm]
Axial length l	130 [mm]
Tip Clearance	0.8 - 0.25 [mm]
Inlet blade angle at tip β1t	63 [degree]
Outlet blade angle β2	30 [degree]

This impeller is not the most advanced design but has been extensively studied and been used to verify the modeling methods [22-24]. The impeller flow is subsonic under most conditions. For the design point condition of 14000 RPM and a mass flow of 5.31 kg/s, the inlet tip relative Mach number is 0.683 and the outlet Reynolds number is 6.12x10⁵.

ANSYS CFX (19.2) is used in all the CFD simulations in this work. It uses an element-based finite volume method and a pressure-based coupled solver approach. The solution variables and fluid properties are stored at the nodes (mesh vertices). A tri-

linear element shape function is employed to interpolate the diffusion term and a linear-linear interpolation shape function is used for the pressure gradient terms. A high-resolution advection (2nd order accuracy) is used with the SST turbulence model. As discussed before, the near wall entropy generation is high, especially where y + is below 10. In the k- ε turbulence model wall functions were developed for the near wall region but those wall functions were not designed for the entropy production terms. The entropy generation near the wall can be seriously underpredicted using k-ε turbulence model with wall functions. Kock and Herwig [3] developed special wall functions for the entropy production terms. But they were not implemented in commercial CFD tools. Instead the SST turbulence model is employed in this work and no wall functions are needed. A structured mesh is used for the compressor passage with a resolution of y+<3. So, the near wall region entropy generation can be properly captured.

The CFD calculations are performed on the single passage domain under the single-phase steady state assumption. The working fluid is air ideal gas. Total pressure and total temperature are specified at the domain inlet with the flow direction normal to the inlet plane. Massflow rate is specified at the domain outlet. Towards choke condition, static pressure is specified at the outlet. Rotational periodic boundary condition is given in the circumferential direction. For the wall surface, noslip wall boundary condition is specified with smooth wall assumption.

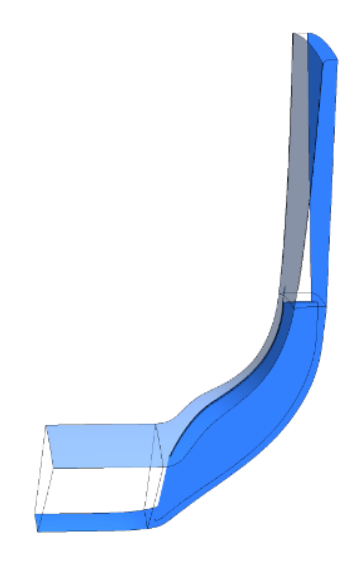


Figure 2. Computational domain of Eckardt A impeller.

The computational domain used in the study is shown in Figure 2. A frozen-rotor method is used at the interface between the rotating domain (impeller) and the stationary domains (inlet block and downstream vaneless diffuser). Figure 3 shows the mesh distribution on the blade surface and on the blade to blade view.

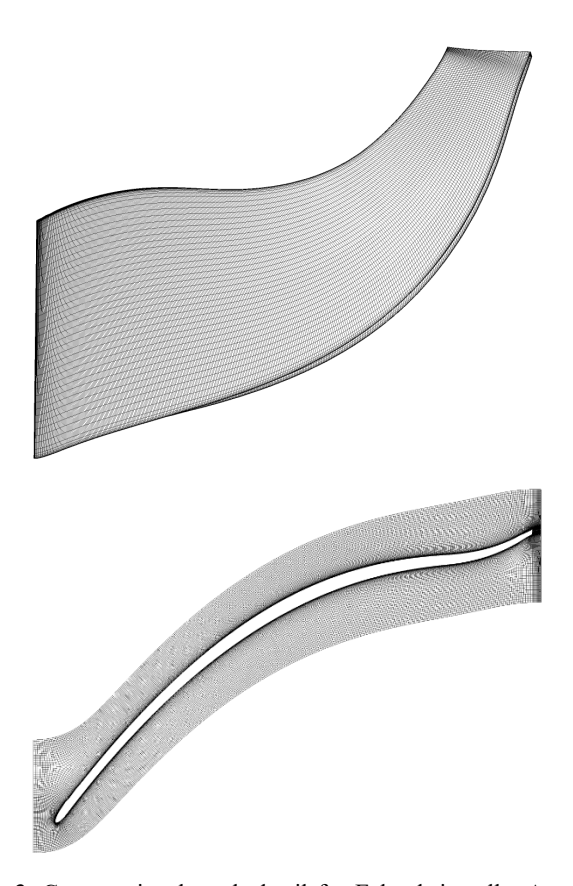


Figure 3. Computational mesh detail for Eckardt impeller A, upper: blade surface mesh; lower: blade to blade view mesh.

Figure 4 shows the CFD predicted pressure ratio (total to total) versus corrected massflow in comparison with the experimental measurements (the experimental data was extracted from the performance map plot in [24]). The outlet total pressure is taken at the same radial position (R/R2=1.69) as in the experimental work. Good agreement is obtained between the measured performance and the CFD predicted speedlines at 12,000 rpm, 14,000 rpm and 16,000 rpm. Towards the stall side the steady state CFD simulation tends to underpredict the stall margin, especially at high rotational speeds. The CFD prediction gives slightly higher pressure ratio at high flow rate. In the experimental work a throttle ring was mounted near the outlet of the diffuser [20], which was used to eliminate the distortion from downstream of the vaneless diffuser. This is not modeled in the CFD study and can cause some difference. Overall, the numerical prediction matches the measured performance quite well at all three rotational speeds.

Performance Map of Eckardt Impeller A

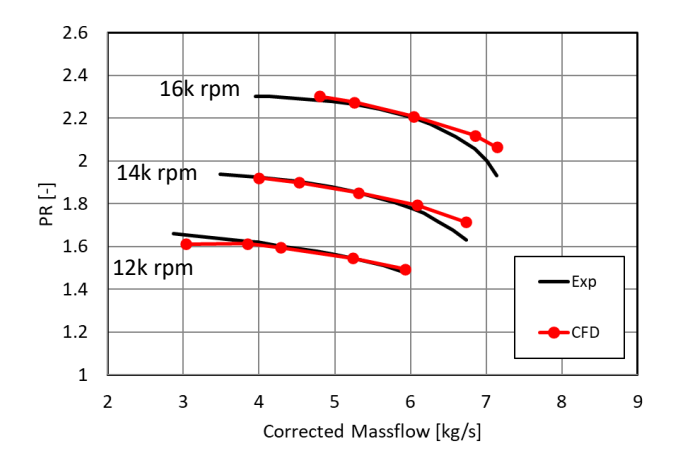


Figure 4. Comparison of predicted and measured total to total stage pressure ratio versus corrected massflow for Eckardt impeller A.

The mesh used in the speedline calculation was arrived at after a mesh sensitivity study. The total entropy generation rate in the impeller can be achieved from volume integration over the impeller domain:

$$\dot{S} = \int_{Imp} \dot{S}_{vol} \, dV \tag{16}$$

A coarse, medium, medium fine and a fine mesh were tested at 14000 rpm and 5.31 kg/s. Table 2 shows the size of the different meshes and the calculated entropy generation rate in the impeller. As mentioned before, for an adequate calculation of the near wall entropy generation, a high resolution of the boundary layer is required. As such, y + is kept small for all mesh levels. It can be observed that as the mesh is refined the predicted entropy generation rate increases. The result of the 'medium fine' mesh converges to that of the 'fine' mesh. In Figure 5 the entropy generation rate is normalized by the value from the fine mesh prediction. It shows the difference between the 'medium fine' mesh result and the 'fine' mesh result is less than 1%. The 'medium fine' mesh was chosen for the speedline simulations considering the balance between the accuracy and the computational resource.

Table 2. Mesh sensitivity study for the Eckardt "A" impeller.

	Mesh Elements [million]	Yplus [-]	\dot{S} [W/(m ³ K)]
Coarse	2.2	<5	1.781
Medium	4.2	<3	1.898
Medium Fine	6.2	<3	1.940
Fine	9	<3	1.957

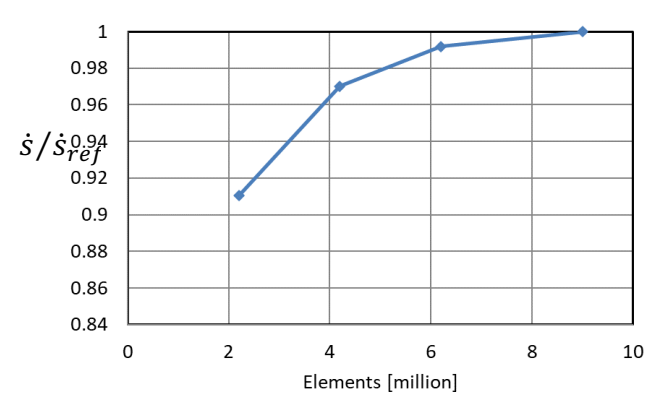


Figure 5. Calculated impeller entropy generation rate versus mesh size for Eckardt impeller A.

The same study has been done for the second compressor. It is a high pressure ratio transonic centrifugal compressor with splitter blades [26] [27]. The impeller was denoted as SRV2AB. Performance measurements and laser measurements along the impeller passage was carried out in previous experimental work. The key geometrical information is listed in Table 3. For the design point condition of 50000 RPM and a mass flow of 2.71 kg/s, the inlet tip relative Mach number is 1.34 and the outlet Reynolds number is 8.3x10⁵.

Table 3. Geometry of the "SRV2AB" impeller

Number of blades Z	13 (full) + 13 (splitter)
Impeller diameter D2	224 [mm]
Impeller outlet width b2	8.7 [mm]
Inlet shroud radius r1s	78[mm]
Axial length l	130 [mm]
Tip Clearance	0.5 - 0.3 [mm]
Inlet blade angle at tip β1t	63.5 [degree]
Outlet blade angle β2	52 [degree]

The numerical study setup is the same as what was used for the Eckardt impeller A. The computational domain consists of an inlet block, the rotating impeller domain and the stationary vaneless diffuser domain. Figure 6 shows the mesh distribution on the impeller blade surface and on the hub. This mesh was used to calculate the speedline performance. The results are compared to test data in Figure 7.

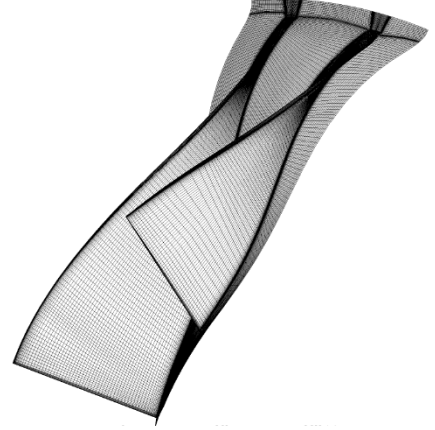
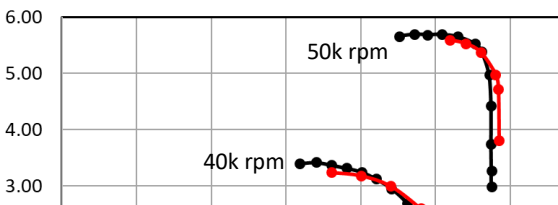


Figure 6. Computational mesh detail for SRV2AB impeller

The predicted pressure ratio is compared to the measured value at two different rotational speeds: 40,000 rpm and 50,000 rpm. The general agreement between the CFD results and test data is good. Again, the steady state CFD underpredicts the stall margin, especially at high rotational speeds. The choke margin is slightly higher compared to the test data.



Performance of SRV2AB Impeller

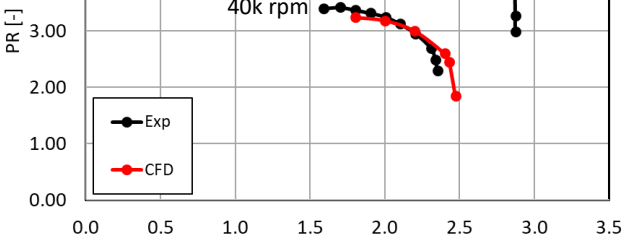


Figure 7. Comparison of predicted and measured total to total stage pressure ratio versus corrected massflow for SRV2AB impeller.

Corrected Massflow [kg/s]

A mesh sensitivity study has also been carried out (at 40,000 rpm and 2.4 kg/s) for SRV2AB impeller for 5 different mesh densities. The results are shown in Table 4. Again, as the mesh is refined the predicted value of the entropy generation rate in the impeller domain converges. It is obvious that with the coarse mesh and a y + higher than 20 the entropy generation rate cannot be accurately captured. On the other hand, the predicted pressure ratio is less dependent on the mesh density and the near wall resolution. All the meshes give a pressure ratio within 2% difference compared to the 'very fine' mesh data. The 'fine' mesh predicts the entropy generation rate with 2.3% difference compared to the 'very fine' mesh. The speedline studies are carried out with this mesh level to maintain the accuracy with a modest computational time.

Table 4. Mesh sensitivity study for SRV2AB impeller.

	Mesh Elements [million]	Yplus [-]	<i>Š</i> [W/(m3K)]	PR [-]
Coarse	2.275	<25	2.882	2.586
Medium	3.927	<4	4.143	2.566
Medium Fine	5.352	<2	4.448	2.575
Fine	9.633	<1	4.608	2.598
Very Fine	13.079	<1	4.719	2.615

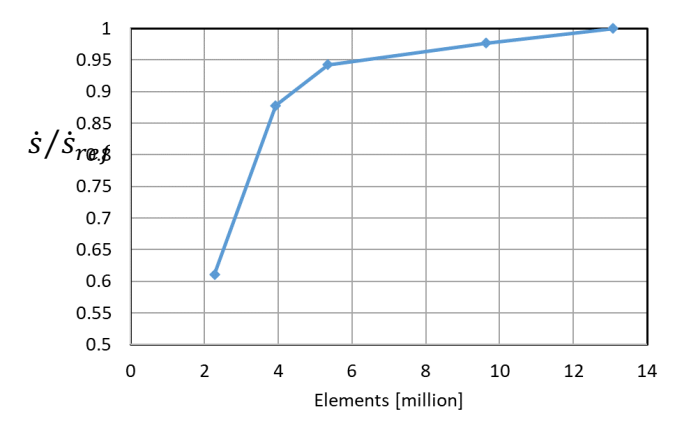


Figure 8. Calculated impeller entropy generation rate versus mesh size for SRV2AB impeller.

After the validation of the numerical simulations, a detailed loss analysis using the methodology introduced in the previous section is conducted for both compressors. The results will also be compared to an optimized design in both cases. The impact of design optimization can be analyzed through entropy generation study.

5. SUBSONIC CENTRIFUGAL COMPRESSOR

The flow field measurement by Eckardt was mainly carried out at 14,000 rpm. The loss analysis is carried out at the same rotational speed. The domain analyzed is the impeller passage. TE wake mixing loss and the diffuser loss are not part of the current study.

Since the Eckardt impeller A is functioning under subsonic flow conditions, little loss is expected from the irreversible shock wave. In fact, only a small region at the impeller LE near the shroud has slightly higher Mach number. Towards high flow rate conditions this region is more visible as the inlet velocity is increased. Figure 9 shows the zone picked up by the shock wave identification method at the highest flow rate on the speedline (6.73 kg/s). It can be seen from the blade-to-blade view (Figure 9, right) that only a small region at the pressure side near LE has Mach number over 1.0. The volume shown in Figure 9 left picked up the mesh elements near this region and it is identified

as 'shock zone'. In the tip clearance part, there is also small region that is picked up by this criterion. But overall, the shock wave is not prominent in the flow field.

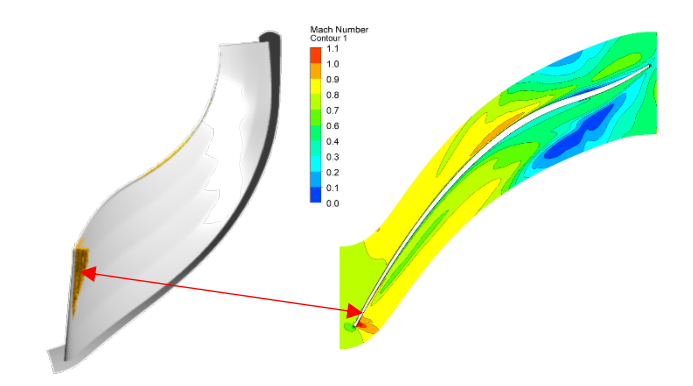


Figure 9. Shock identification for Eckardt impeller A at 6.73 kg/s, left: shock zone; right: 95% span Mach number distribution in blade-to-blade view.

The boundary layer zone is mainly detected by the near wall high turbulence eddy dissipation. Figure 10 shows the regions identified as boundary layer in the impeller passage. The thin blue zone in Figure 10 (upper) is near the blade surface and at the hub and shroud end wall. It is separated from the fluid domain by limiting the turbulence eddy dissipation value. The turbulence eddy dissipation at mid span is shown on a blade-toblade view in Figure 10, lower. It is obvious that the near wall region has a high value compared to the mainstream flow. Towards the trailing edge the vortex in the passage also causes regions of high eddy dissipation. These regions were excluded from the boundary layer zone. It can also be observed that near the hub, part of the area is not picked up by the boundary layer identification. This is because the endwall vortex is acting on that specific area hence it is categorized as part of the secondary flow zone rather than the boundary layer zone. From the blade-toblade view it can also be observed that the boundary layer grows more rapidly on the suction surface of the impeller blade and it has slightly thicker boundary layer than the pressure surface.

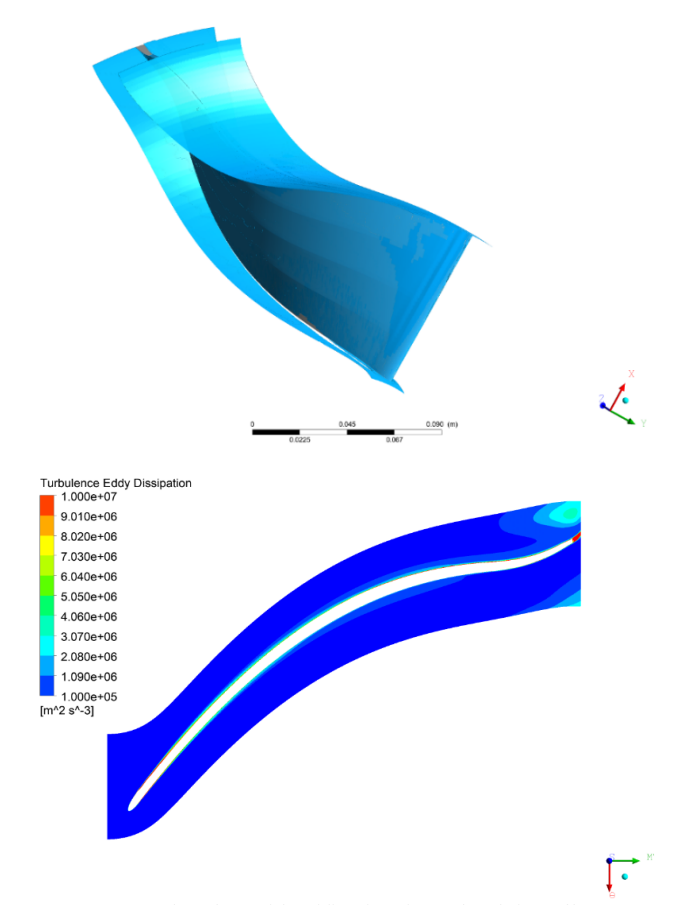


Figure 10. Boundary layer identification for Eckardt impeller A at 5.31 kg/s, upper: boundary layer zone; lower: 50% span turbulence eddy dissipation distribution in blade-to-blade view

To find the secondary flow zone in the impeller passage vortex identification techniques are used, together with flow visualization. Figure 11 (upper) shows the contour plot of velocity variant Q (the passage was copied several times along the annulus to show the flow structure). The area with high vorticity is highlighted by red. The 3D streamlines (Figure 11, middle) show that strong secondary flow develops inside the passage moving the fluid from hub to shroud. Both suction and pressure surfaces have flow going to the shroud. At the trailing edge a large high entropy vortex is formed near the shroud. The elements belonging to the secondary flow structure are captured and separated from the main flow (Figure 11, lower). It can also be seen that near the blade leading edge the horseshoe vortex and the endwall vortex are also picked up by this criterion.

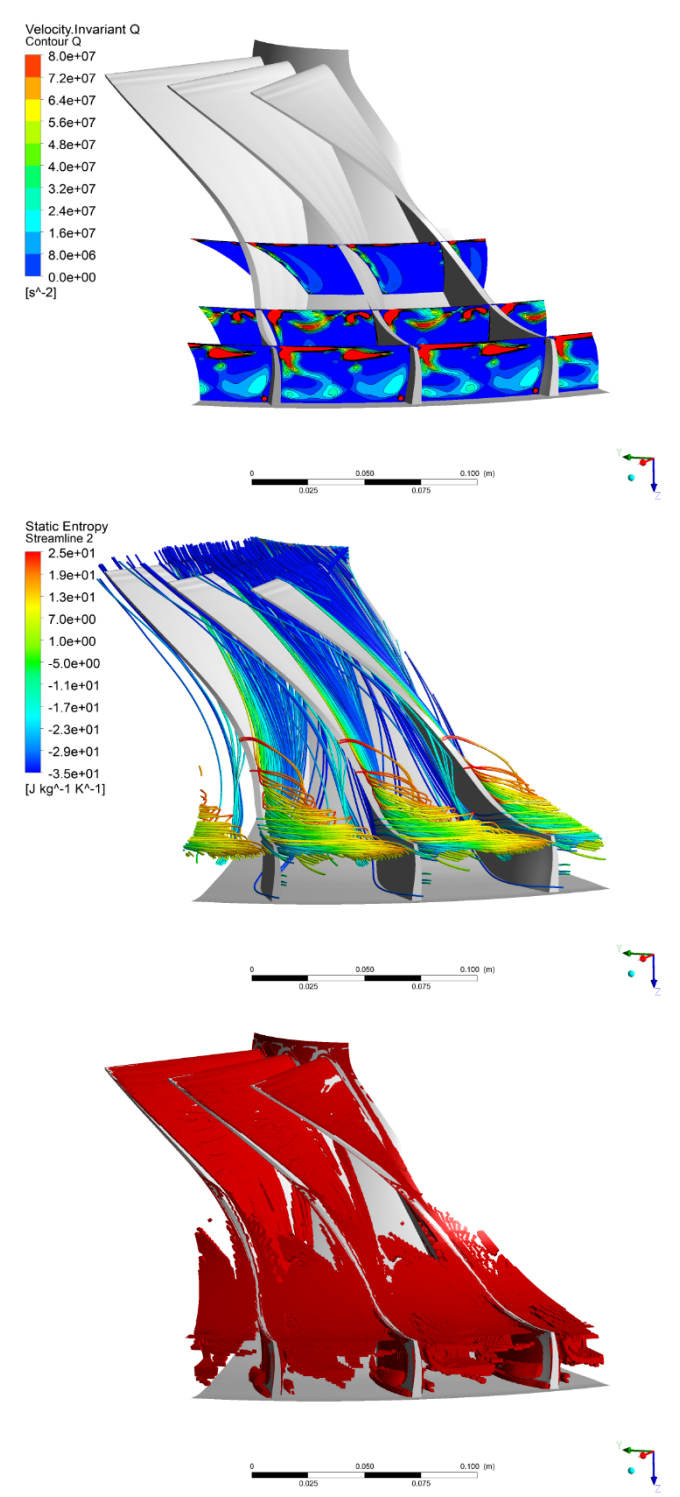


Figure 11. Secondary flow identification for Eckardt impeller A at 5.31 kg/s, upper: contour of velocity invariant Q; middle: 3D streamlines colored by entropy, lower: secondary flow zone.

The last category is tip leakage loss. As mentioned before, it is separated from other vortices in the passage by the absolute helicity and turbulence kinetic energy. The result is shown in Figure 12. The tip flow moves from pressure side to suction side,

over the blade tip and propagates towards the adjacent blade. The tip leakage zone captured and separated this flow structure from the rest of the passage.

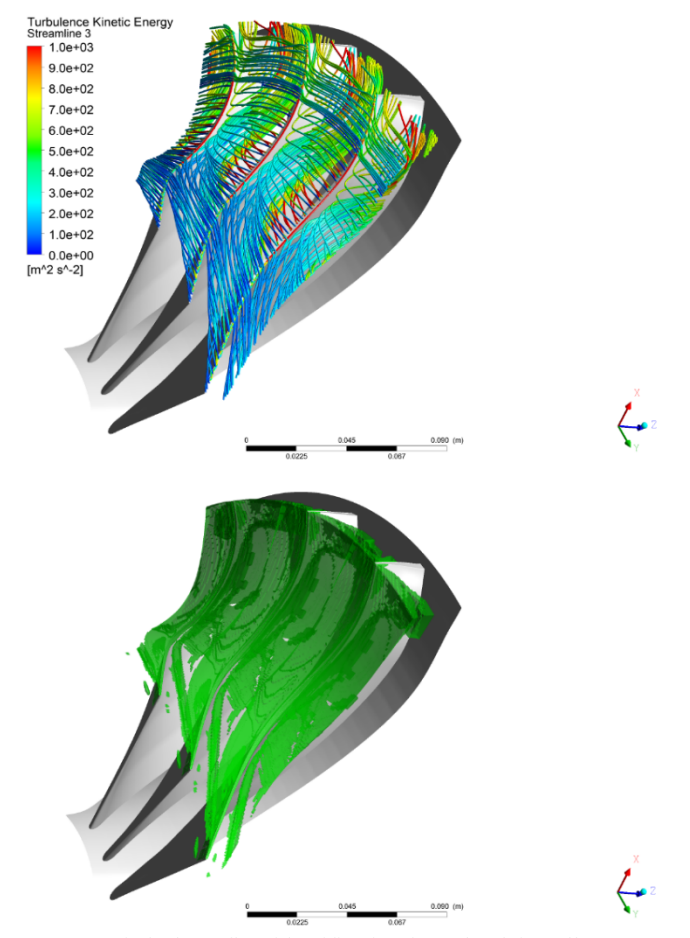


Figure 12. Tip leakage flow identification for Eckardt impeller A at 5.31 kg/s, upper: 3D streamlines colored by turbulence kinetic energy, lower: tip leakage flow zone.

The demonstration on Eckardt impeller A shows the flow field has been decomposed into different regions by the criteria used. Each region captured the flow that accounts for a certain type of loss. By integrating the entropy generation rate per volume over these zones, the loss created by each flow feature can be quantified.

Firstly, the total entropy generation rate is computed for the impeller passage at various flow rates. The four terms in Equation 2 are shown on a stacking plot in Figure 13. It is apparent that most entropy generation is associated with the viscous dissipation occurring due to the turbulence fluctuations. It contributes to over 75% of the total entropy generation. The viscous dissipation from mean flow also creates a considerable portion of entropy generation, whereas the heat flux terms have little contribution. The entropy generation from heat flux of the mean flow is negligible compared to other terms. Towards high flow rate conditions the overall entropy generation increases with each term progressively producing more entropy.

Entropy Generation Rate vs Flowrate

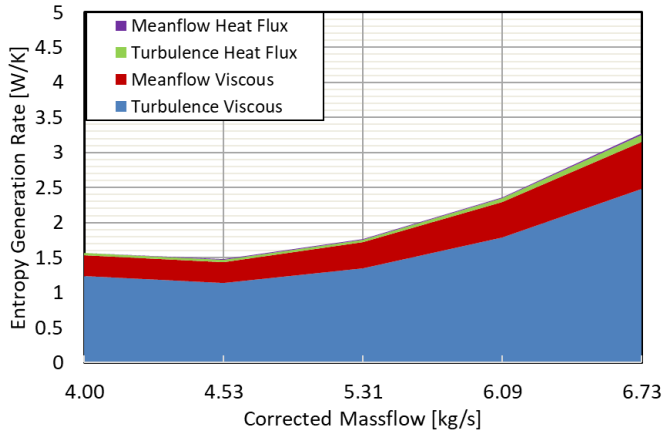


Figure 13. Entropy generation rate (decomposed by production terms) versus corrected masslfow for Eckardt impeller A.

Figure 14 shows the breakdown of entropy generation based on the fluid zones identified by different mechanisms. The decomposition is also plotted against the corrected massflow. As expected, the boundary layer zone produces more entropy at high flow rate since the velocity close to the wall is relatively high. The secondary flow also contributes towards a large portion of the overall entropy generation. At high flow rate conditions, it produces more than a third of the total entropy generation. The tip leakage flow produces similar portion of entropy generation in comparison to the secondary flow and the boundary layer flow. It also increases slightly at high flow rate conditions. The entropy generated by the shock wave is negligible except at the highest flow rate (shown in Figure 9). The sum of the entropy generation from the four categories has the same distribution as in Figure 13. In fact, over 90% of the total loss is captured by these categories. There is some remaining loss in the part of the passage flow not covered by the 4 categories discussed.

Entropy Generate Rate vs Flowrate

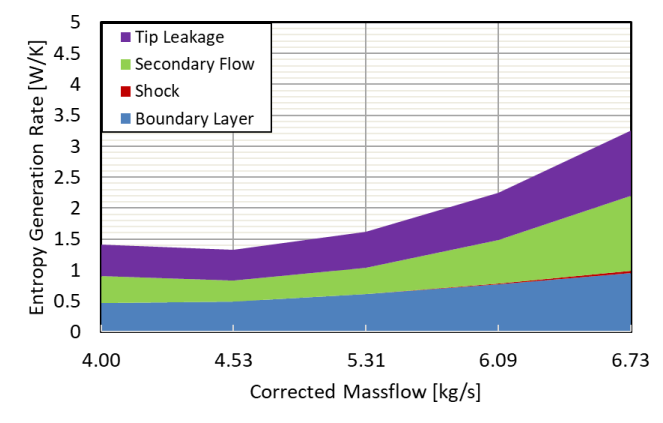


Figure 14. Entropy generation rate (decomposed by sources) versus corrected masslfow for Eckardt impeller A.

5.1 Design Optimization

After the loss analysis on the flow field of the Eckardt impeller A was obtained, an optimization was carried out with a 3D inverse design tool TURBOdesign1 [28]. The tool has been applied to compressors and pump designs extensively. The inverse design method uses a 3D inviscid flow solver and can solve for both compressible and incompressible flow. The solver provides both the blade geometry and 3D inviscid flow field solution that compares well with CFD results. The theory of the method was introduced in the early work by Zangeneh [16] [17].

The advantage of the inverse design method is that the blade geometry is controlled by the aerodynamic inputs which are related to the flow behavior. The circumferentially averaged bound circulation is used as input to specify the blade loading. It is defined as:

$$r\overline{V_{\theta}} = \frac{N}{2\pi} \int_{0}^{2\pi/N} r \cdot V_{\theta} d\theta \tag{17}$$

The Euler head (work coefficient) can be fixed by specifying the spanwise $r\overline{V_{\theta}}$ distribution at the leading edge and trailing edge of the blade.

Meanwhile, the meridional derivative of $r\overline{V_{\theta}}$ is related to the pressure difference between the blade pressure surface and suction surface:

$$p^{+} - p^{-} = \frac{2\pi}{N} \rho W_{mbl} \frac{\partial (r\overline{V_{\theta}})}{\partial m}$$
 (18)

By prescribing the meridional derivative $\partial(r\overline{V_{\theta}})/\partial m$ (blade loading) in the blade passage the corresponding blade geometry can be computed by the inverse design procedure. Therefore, the blade geometry is controlled by the pressure field which is prescribed as an input.

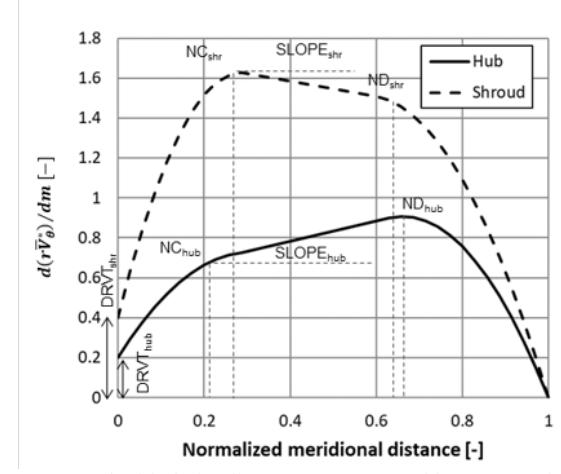


Figure 15. The blade loading parameters used in TURBOdesign1

Figure 15 shows the required blade loading parameters to generate the blade geometry. $r\overline{V_{\theta}}$ is normalized by the impeller outlet tip radius and speed. The normalized value $(r\overline{V_{\theta}}^*)$ is used to specify the loading. Three segments (two parabolic curves and a linear line connecting the two) are used on the hub and shroud streamlines. Four parameters (NC, ND, SLOPE and DRVTLE) are needed to define a loading curve. The value of DRVTLE $(\partial(r\overline{V_{\theta}}^*)/\partial m)$ at the leading edge) affects the blade incidence and the peak efficiency point of the design. Therefore only 8

parameters are needed to define a complex 3D blade shape. In addition, the stacking condition can be specified at a chordwise location between the blade leading edge and trailing edge. The stacking condition is used as an initial condition in the inverse design code. It is introduced by specifying variation of wrap angle from hub to shroud at one quasi-orthogonal location (usually taken at trailing edge for centrifugal impellers). This adds one additional parameter to control the spanwise pressure field.

Once the solver converges on a solution the pressure and velocity distribution on the blade surface will be available. Some performance parameters can be deduced with this information to evaluate a design before running more time consuming CFD analysis. Since the inverse design solver converges on a single core within a few seconds, it can be coupled to an optimizer to explore the design space quickly. The parameterization by blade loading also reduces the degree of freedom needed to describe a blade geometry. The optimization work on Eckardt impeller is carried out within TURBOdesign Suite [29] using its embedded genetic optimizer (TDOptima). A direct multi-objective genetic algorithm optimization is conducted.

As shown in Figure 14, the boundary layer friction and secondary flow produce the major portion of total loss. Therefore, the objectives are set to minimize the profile loss and the secondary flow factor. The profile loss factor is computed from the integration of the cube of the blade surface velocity predicted by the inverse design code. Previous work [1] shows that the entropy generation on the blade surface is largely proportional to this value:

$$\dot{S} = \int_0^x \frac{\rho V_\delta^3 C_d}{T_\delta} dx \tag{19}$$

The secondary flow factor is characterized by the loading difference between the hub and the shroud. It is related to the hub-to-shroud motion of fluid. It is calculated in the inverse design code by using the velocity difference (downstream of 50% streamwise location) between the hub and the shroud of the blade. Two constraints are set to rule out the invalid designs. The throat variation range is set to about 2.0% of the baseline value and the diffusion ratio is constrained to avoid flow separation. Table 5 summarizes the range of the input parameters as well as the constraints and objectives used in the optimization.

Table 5: Optimisation inputs, objectives and constraints

Variables	Range
NChub	0.2-0.4
NDhub	0.6-0.9
SLOPEhub	0.5-1.75
DRVThub	-0.5-0.5
NCshr	0.2-0.4
NDshr	0.6-0.9
SLOPEshr	-0.25-0.5
DRVTshr	-0.5-0
Stacking	-5-5 [deg]

Constraints	
Throat	±1%
Diffusion Ratio	1.5-1.74
Objectives	
Profile loss	Minimize
Secondary flow factor	Minimize

Direct Optimization with Inverse Design Code

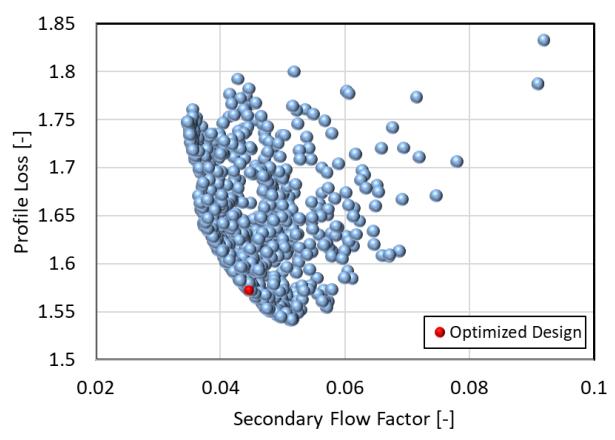


Figure 16. Profile loss against secondary flow factor in optimization.

In total, 1178 feasible inverse design solutions have been generated. The results are plotted in Figure 16. It is obvious that minimizing profile loss and minimizing secondary flow are contrasting objectives and a Pareto front of the two objectives can be observed. From the Pareto front a final design (marked by the red bubble) is selected. It is denoted as the optimized design.

Streamwise Blade Loading Distribution

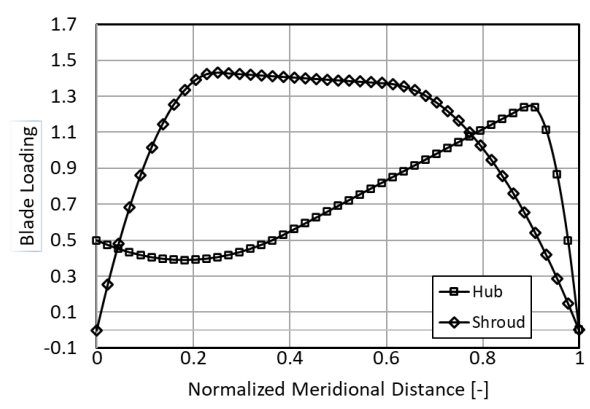
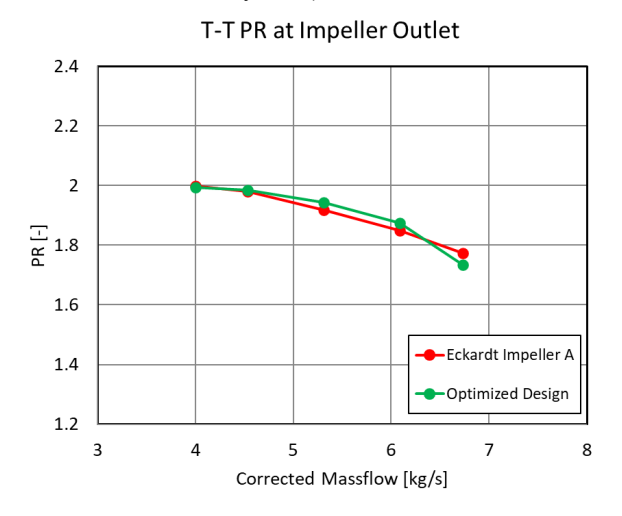


Figure 17. Loading distribution on hub and shroud blade surface for the optimized design

The loading distributions of the optimized design are shown in Figure 17. It can be seen that the hub is very aft-loaded. In addition, stacking is also applied in the optimized design, with the hub wrap angle leading the shroud wrap angle by 5 degrees. This type of loading and stacking distribution have proven to be effective in suppressing the secondary flow in centrifugal machines [11]. This is attributed to the minimization of the

loading difference between hub and shroud at the second half of the meridional distance. The reduced static pressure difference between the hub and shroud (which is the driving force of the hub-to-shroud secondary flow) is therefore minimized.



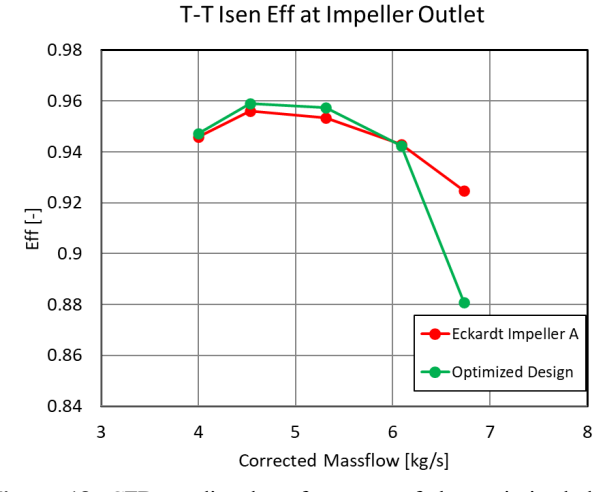


Figure 18. CFD predicted performance of the optimized design at 14,000 rpm in comparison to Eckhardt impeller A, upper: pressure ratio versus flowrate; lower: total-to-total isentropic efficiency versus flowrate.

Figure 18 shows the performance prediction (at 14,000 rpm) for the optimized design by CFD analysis. It uses the same numerical setup as described for the Eckardt impeller A. As the loss analysis is done in impeller domain only the impeller performance (shown in Figure 18) was calculated at the impeller outlet. The loss from downstream vaneless diffuser is not included. The comparison shows that the optimized design delivers similar pressure ratio across different flowrate conditions. The efficiency of the impeller is improved at the design point (5.31 kg/s) and lower flow rate. Towards high flow rate condition, the efficiency drops slightly compared to the original design.

The entropy generation rate by each production term is shown on a stacking plot in Figure 19. It can be observed that the

total entropy generation rate is reduced at the design condition and lower flowrates compared to Figure 13. The minimum of the total entropy generation rate corresponds to the peak efficiency point in Figure 18. The reverse of the entropy generation rate resembles the efficiency characteristics.

Entropy Generation Rate vs Flowrate 5 ■ Meanflow Heat Flux 4.5 ■ Turbulence Heat Flux Entropy Generation Rate [W/K] ■ Meanflow Viscous 4 ■ Turbulence Viscous 3.5 3 2.5 2 1.5 1 0.5 0 5.31 6.09 6.73 4.00 Corrected Massflow [kg/s]

Figure 19. Entropy generation rate (decomposed by production terms) versus corrected masslfow for the optimized design (subsonic).

Figure 20 shows the breakdown of entropy generation for the optimized design. Compared to Figure 14 the boundary layer zone produces similar entropy. The main reduction of entropy generation is from the secondary flow and the tip leakage flow. Apart from the highest flow rate condition the entropy generated by shocks is not obvious.

Entropy Generate Rate vs Flowrate

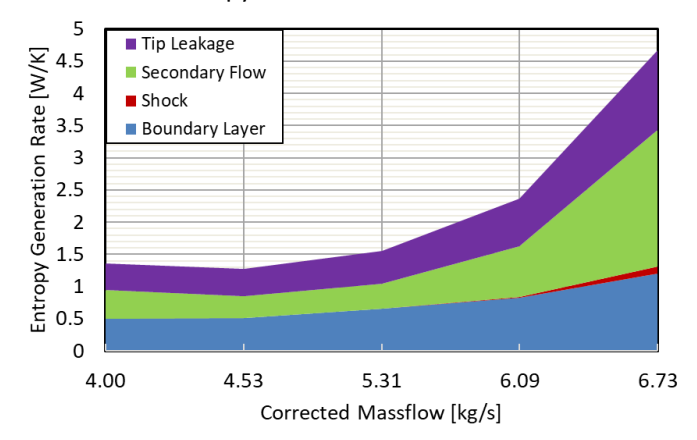


Figure 20. Entropy generation rate (decomposed by sources) versus corrected massflow for the optimized design (subsonic).

Figure 21 shows the contour plot of velocity variant Q in the passage of the optimized design (at 5.31 kg/s). Compared to Figure 11(upper) the high vorticity area (highlighted by red) at the trailing edge of the impeller is greatly reduced. The reduction of vortices in the passage (especially near the shroud) results in less loss created by secondary flow and the tip leakage vortex. This is consistent with the reduced entropy generation rate by secondary flow and by tip leakage shown in Figure 20.

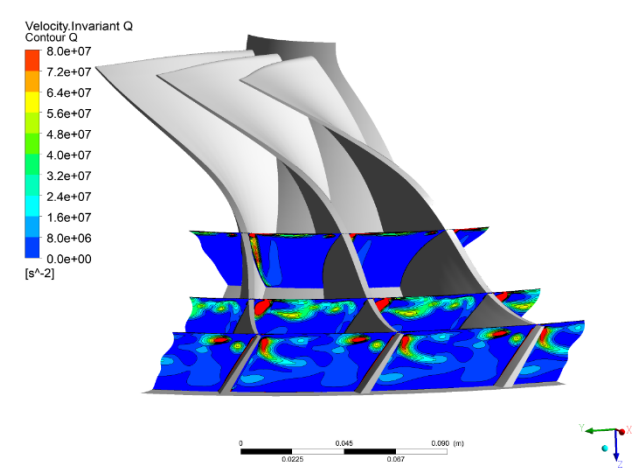


Figure 21. Contour of velocity invariant Q for optimized design at 5.31 kg/s.

Towards the choke condition, entropy generation in secondary flow grows rapidly in Figure 20. Besides, it is noticed that the shock loss is increased. This is due to the higher local Mach number. The stronger shock wave also induces strong loss in secondary flow, which contributes to the drop of efficiency.

The demonstration and analysis on Eckardt impeller and optimized design show that the proposed methodology well captures the losses under different flow conditions. It can also pick up the influence from design optimization. Using the analysis through entropy generation rate, a good understanding of the loss mechanism inside the impeller can be achieved, which helps to carry out targeted performance optimization.

6. TRANSONIC CENTRIFUGAL COMPRESSOR

The same loss breakdown analysis was carried out for both the SRV2AB impeller and its TURBOdesign1 optimized design. For high-pressure-ratio centrifugal compressors, the inlet relative Mach number near the shroud is high. It becomes supersonic and strong shock waves can form at the blade inducer if not designed carefully. Thus, the optimization needs to take into consideration the shock loss as well as other losses. This makes the design more complex compared to subsonic compressors. The optimized design was produced by Zangeneh et al. [30]. It shows a 2-2.5% improvement of stage efficiency at different rotational speeds. The optimized design uses a strongly aft-loaded hub and mildly aft-loaded shroud (Figure 22). It provides a good compromise between suppression of secondary flow and decreasing the shock losses.

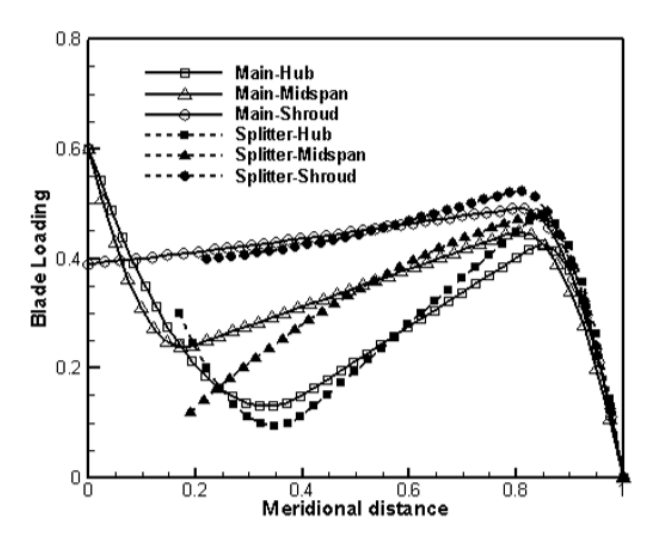
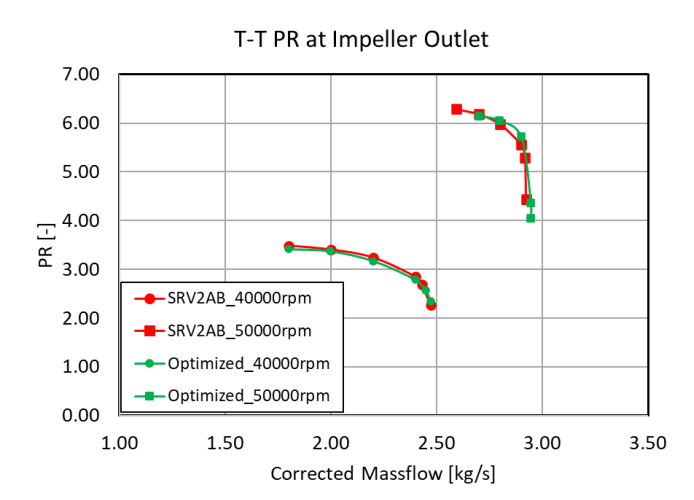


Figure 22. Loading distribution on hub, midspan and shroud of the main and splitter blade for the optimized design (Zangeneh et al. [30]).

The detailed comparison between the original SRV2AB and the optimized design can be found in [30]. Again, the loss analysis is done for the impeller domain only. The impeller performance curves for the two designs are plotted in Figure 23. The loss from the downstream vaneless diffuser is not included. It can be seen that the optimized design has similar pressure ratio to the original design over a range of operating conditions. The efficiency of the optimized design is around 2% higher than the original SRV2AB impeller.



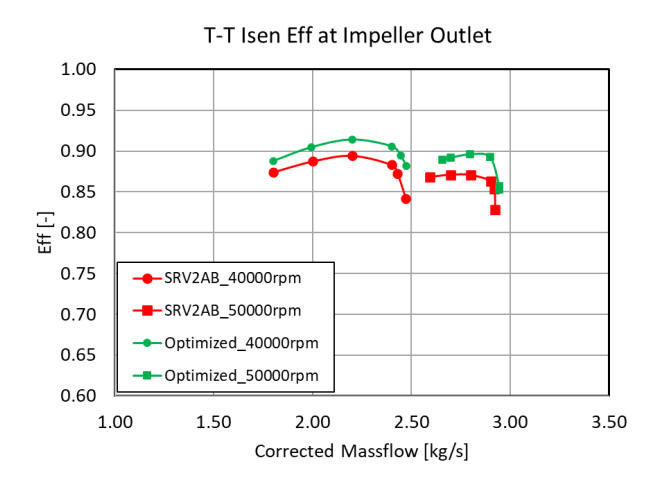
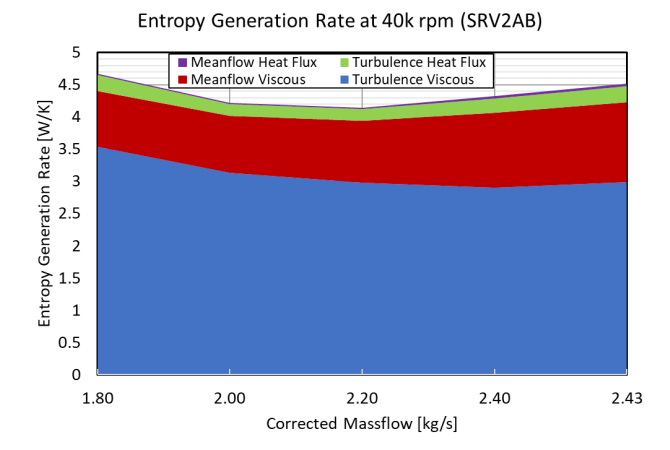


Figure 23. CFD predicted performance of the optimized design in comparison to SRV2AB impeller, upper: pressure ratio versus flowrate; lower: total-to-total isentropic efficiency versus flowrate

The entropy generation of both designs was extracted to better understand the impact of design modification and to quantify the change in different loss contributions. Figure 24 shows the comparison of entropy generation rate at 40,000 rpm between the SRV2AB impeller and the optimized design. The same as shown in Figure 13, most entropy generation is created by the viscous dissipation from the turbulence fluctuation. The viscous dissipation from mean flow creates another major portion of entropy generation. The heat flux terms have little contribution. Towards off-design conditions the overall entropy generation increases, which corresponds to the efficiency drop seen on the speedline (Figure 23). It is also clearly demonstrated that the optimized design reduces the entropy generation rate at all conditions, which is in agreement with the overall higher efficiency observed in Figure 23.



Copyright © 2020 by ASME

Entropy Generation at 40k rpm (Optimized)

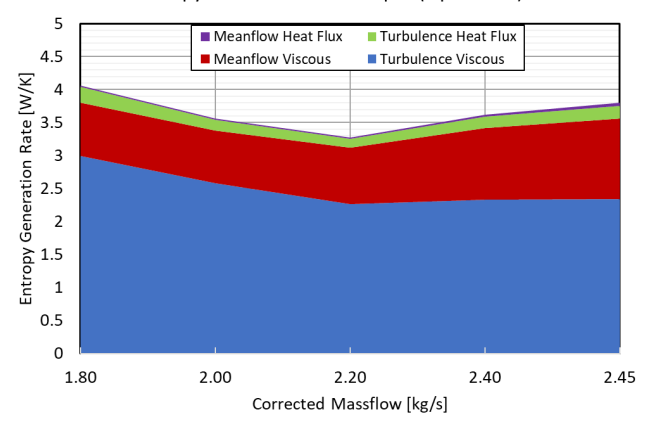
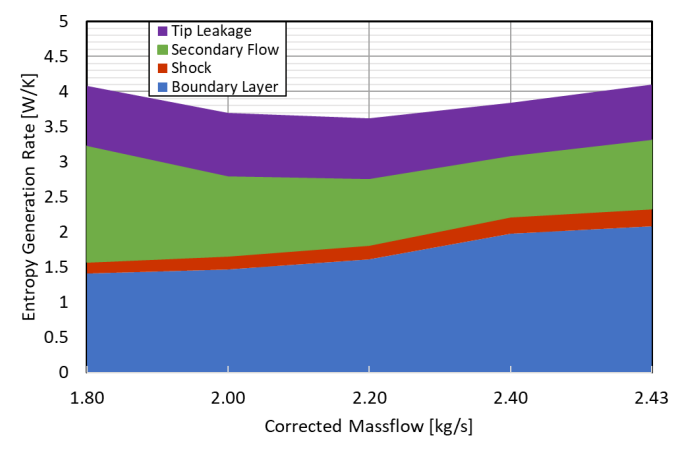


Figure 24. Entropy generation rate (decomposed by production terms) versus corrected masslfow for the SRV2AB impeller and the optimized design (40k rpm), upper: SRV2AB, lower: Optimized Design.

The breakdown of entropy generation by different mechanisms is shown in Figure 25. Similar to the Eckardt impeller A analysis the entropy generation in boundary layer increases with massflow. The shock loss however is not negligible in both the SRV2AB impeller and its optimized design. The shock loss also increases with massflow as the flow Mach number is increased. The optimized design reduces the shock loss towards the choke condition. But the major reduction of entropy generation is from the secondary flow. The optimized design significantly reduces the secondary flow loss, especially towards high flow rate conditions. Since secondary flow contributes a big portion of the overall entropy generation, suppressing the secondary flow in the impeller passage effectively improves the efficiency. The tip leakage flow also produces an important portion of entropy generation but the change with massflow is not very big.

Entropy Generation Rate at 40k rpm (SRV2AB)



Entropy Generation Rate at 40k rpm (Optimized)

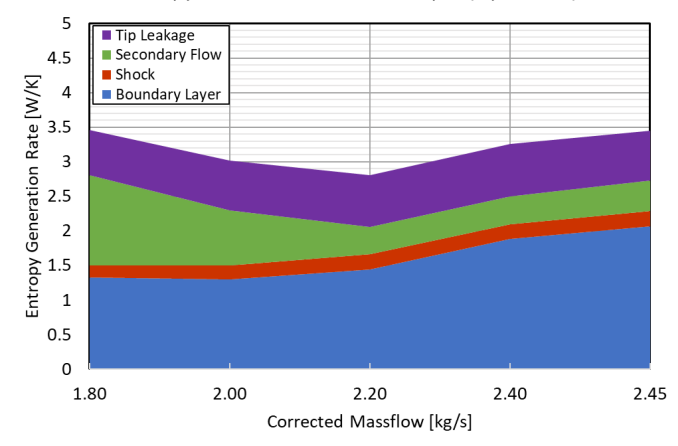
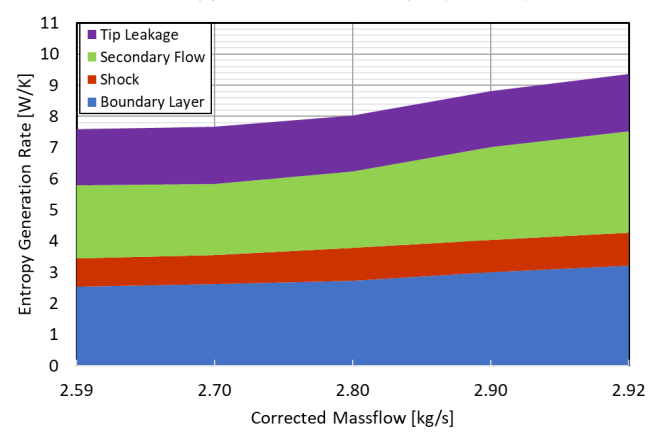


Figure 25. Entropy generation rate (decomposed by sources) versus corrected masslfow for the SRV2AB impeller and the optimized design (40k rpm), upper: SRV2AB, lower: Optimized Design.

Figure 26 shows the breakdown of entropy generation by difference mechanisms at 50,000 rpm. Compared to Figure 25 the overall entropy generation level is almost twice the value at 40,000 rpm. In addition, the shock loss is much higher at high rotational speed. The optimized design reduces the shock loss visibly at all flowrates. The secondary flow is also greatly reduced by the design optimization. Both contribute to the improvement of efficiency shown in Figure 23.

Entropy Generation at 50k rpm (SRV2AB)



Entropy Generation at 50k rpm (Optimized)

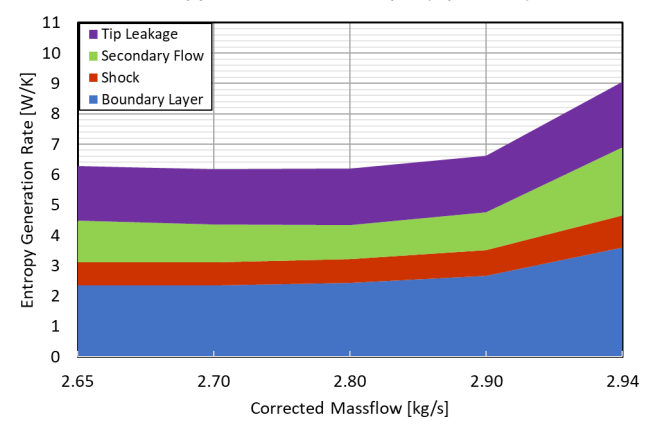


Figure 26. Entropy generation rate (decomposed by sources) versus corrected masslfow for the SRV2AB impeller and the optimized design (50k rpm), upper: SRV2AB, lower: Optimized Design.

At the design point 2.7kg/s the entropy generation breakdown is compared between the two designs (Figure 27). It is evident that the strongly aft-loaded hub and mid aft-loaded shroud loading distribution for the main blade has effectively suppressed the secondary flow. Meanwhile the shock loss is also reduced.

Entropy Generation Rate at 2.7 kg/s, 50krpm

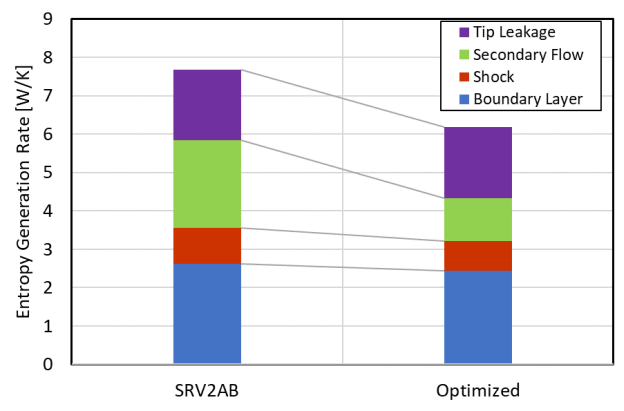


Figure 27. Entropy generation rate (decomposed by sources) at 2.7kg/s for the SRV2AB impeller and the optimized design (50k rpm).

The shock zone captured by the identification method is shown in Figure 28. It can be seen that near the leading edge the shock zone is reduced from mid-span to hub in the case of the optimized design. This is due to the reduced loading at the hub and mid-span in the inducer area.

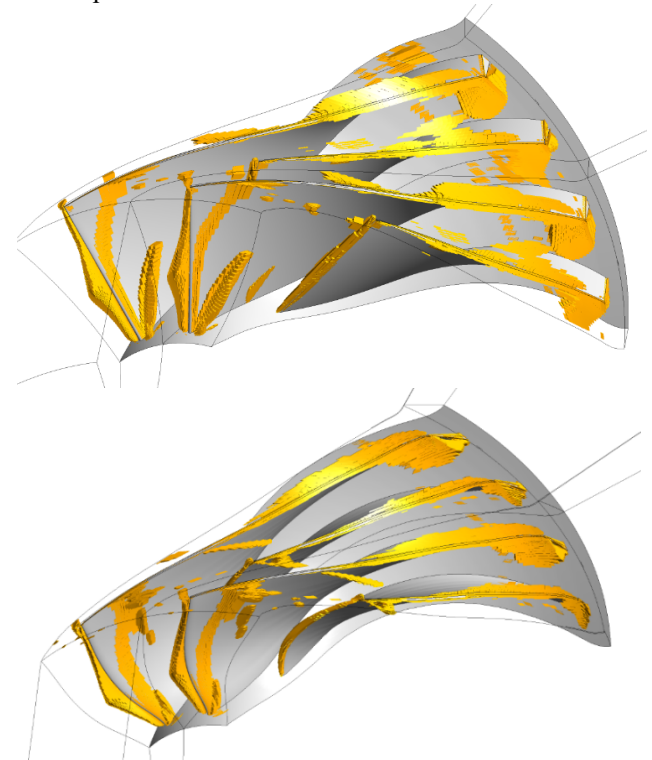


Figure 28. Shock identification for SRV2AB impeller and the optimized design at 2.7 kg/s, upper: SRV2AB; lower: Optimized Design.

The analysis on SRV2AB impeller and optimized design shows that for transonic centrifugal compressors it is important to suppress the shock wave. The proposed method captures the shock loss and the change in its magnitude as a result of design optimization. By using careful loading control, it is possible to limit both shock wave loss and secondary flow loss. These can lead to considerable improvement in performance.

7. CONCLUSION

In this paper a loss evaluation method is developed to quantify the loss creation based on entropy generation. The breakdown of different loss mechanisms is obtained by separating the fluid domain into different zones. The underlying flow physics for the flow decomposition are discussed. The method is demonstrated on two centrifugal compressor examples. The entropy generation rate from each loss mechanism is extracted from the flow field under various operating conditions. For the subsonic compressor (Eckardt impeller A) an optimization is carried out based on the loss analysis results. It shows by suppressing the passage secondary flow and limiting the blade profile loss the impeller peak efficiency can be improved. For the transonic compressor (SRV2AB) the suppression of shock loss as well as the secondary flow loss improves the efficiency considerably. The entropy generation analysis enables the designers to get a good understanding of the loss mechanisms inside the impeller. With the knowledge of the loss decomposition it is possible to carry out targeted optimization using the inverse design method, which can control the flow field of a specific design through blade loading distribution.

8. DISCUSSION

The methodology developed has been applied to two centrifugal compressors of different scale and speed. The loss breakdown and flow decomposition are done with the help of flow visualization. To make the approach more automatic the criteria used to separate the fluid domain can be linked to some flow parameters. For example, the threshold of turbulence eddy dissipation may be related to the Reynold number of the impeller flow. The helicity and turbulence kinetic energy used to separate the tip leakage vortex flow can be linked to the blade loading and tip gap dimension etc. The modified Rossby number (a measure of centrifugal force to Coriolis force) may be used to estimate the limiting value used in the secondary flow criteria.

The current work focuses on the analysis of entropy generation in the impeller domain. The diffuser domain loss analysis was outside the scope of the current work. However, extending the methodology to the diffuser domain can be very helpful since diffuser generally contributes towards a large portion of the overall loss in a compressor stage. Compared to the impeller the diffuser is quite often a less efficient component. The improvement of diffuser design can largely benefit the stage performance.

Finally, the proposed method can be used to calibrate the loss models used in the design phase. The detailed loss analysis from CFD provides good information for loss model evaluation since it has better spatial resolution and is less expensive than experimental studies.

ACKNOWLEDGEMENTS

Place any acknowledgements here. All running text, including the acknowledgements, should be right-justified, in two columns, single-spaced, and in Times New Roman size 10 font.

REFERENCES

- [1] Denton, J. D., 1993, "Loss Mechanisms in Turbomachines," the 1993 IGTI Scholar Lecture, Ohio USA, Journal of Turbomachinery 115(4), 621-656.
- [2] Moore, J., Moore, J.G., 1983a. "Entropy production rates from viscous flow calculations part i a turbulent boundary layer flow," In: Proc. ASME International Gas Turbine Conference and Expo 1983 83-GT-70. Phoenix, AZ, USA.
- [3] Kock, F., Herwig, H., 2005. "Entropy production calculation for turbulent shear flows and their implementation in CFD codes," Int. J. Heat Fluid Flow 26 (4), 672–680.
- [4] Jin, Y., Du, J., Li, Z. Y., and Zhang, H. W., 2017, "Second-Law Analysis of Irreversible Losses in Gas Turbines," Entropy, 19(9):470.
- [5] Zhao, Y. M., Sandberg, R. D., 2019, "Using a New Entropy Loss Analysis to Asssess the Accuracy of RANS Predictions of an HPT Vane," Proceedings of ASME Turbo Expo 2019: Turbomachinery Technical Conference and Exposition, June 17-21, 2019, Phoenix, Arizona, USA.
- [6] Pullan, G., Denton, J. D. and Curtis, E., 2006, "Improving the Performance of a Turbine With Low Aspect Ratio Stators by Aft-Loading," Journal of Turbomachinery, Jul 2006, 128(3): 492-499
- [7] Newton, P., Copeland, C., Martinez-Botas, R., Seiler, M., 2011, "An audit of aerodynamic loss in a double entry turbine under full and partial admission," International Journal of Heat and Fluid Flow 33 (2012) 70–80.
- [8] Denton, J. D. and Pullan, G. P., 2012, A Numerical Investigation into the Sources of Endwall Loss in Axial Flow Turbines, ASME GT 2012-69173.
- [9] Yoon S., Vandeputte T., Mistry H., Ong J., Stein A., 2016, "Loss Audit of a Turbine Stage," Journal of Turbomachinery, May 2016, 138(5): 051004 (9 pages).
- [10] Johnson, M. W., 1978, "Secondary flow in rotating bends," ASME Journal of Engineering for Power, October 1978, vol. 100, pp. 553–560.
- [11] Zangeneh, M., Goto, A. and Harada, H., 1998, "On the Design Criteria for Suppression of Secondary Flows in Centrifugal and Mixed Flow Impellers," Journal of Turbomachinery, 120(4), 723-735.
- [12] Brun K., and Kurz, R., 2005, "Analysis of Secondary Flows in Centrifugal Impellers," International Journal of Rotating Machinery 2005:1, 45–52.
- [13] Grübel, M., Dovik, R. M., Schatz, M., Vogt, D. M., 2017, "A Methodology for a Detailed Loss Prediction in Low Pressure Steam Turbines," Proceedings of ASME Turbo Expo 2017: Turbomachinery Technical Conference and Exposition, June 26-30, 2017, Charlotte, NC, USA.

- [14] Sun, J., 2014, "Two-phase Eulerian averaged formulation of entropy production for cavitation flow," Ph. D. Thesis, University of Manitoba, Winnipeg, Canada.
- [15] Saito, S., Furukawa, M., Yamada, K., Watanabe, K., Matsuoka, A., Niwa, N., 2019, "Mechanisms and Quantitative Evaluation of Flow Loss Generation in a Multi-stage Transonic Axial Compressor," Proceedings of ASME Turbo Expo 2019: Turbomachinery Technical Conference and Exposition, June 17-21, 2019, Phoenix, Arizona, USA.
- [16] Zangeneh, M., 1991, "A compressible three dimensional Blade design method for radial and mixed flow turbomachinery blades", Int J. Numerical Methods in Fluids, Vol. 13, pp. 599-624.
- [17] Zangeneh, M., 1998, "On 3D inverse design of centrifugal compressor impellers with splitter blades", ASME Paper 98-GT-507.
- [18] Dawes, W. N., 1990, "A Comparison of Zero and One Equation Turbulence Modelling for Turbomachinery Calculations," ASME, International Gas Turbine and Aeroengine Congress and Exposition, 35th, Brussels, Belgium, June 11-14, 1990. 10 p.
- [19] Zaripov, D., Li, R. F., Dushin, N., 2018, "Dissipation rate estimation in the turbulent boundary layer using high-speed planar particle image velocimetry," Experiments in Fluids, (2019) 60:18.
- [20] Eckardt, D., 1976, "Detailed Flow Investigations Within a High-Speed Centrifugal Compressor Impeller," ASME Journal of Fluids Engineering, Vol. 98, pp. 390-402.
- [21] Eckardt, D., 1980," Flow Field Analysis of Radial and Backswept Centrifugal Compressor Impellers Part I. Flow measurements using a laser velocimeter," Performance Prediction of Centnfugal Pumps and Compressors. Gopalakrishnan, ed, ASME publication, pp.77-86.
- [22] Casey, M V. Dalbert, P. and Roth, P. (1992): "The use of 3D Viscous Flow Calculations in the Design and Analysis of Industrial Centrifugal Compressors", Tran. ASME, J. Turbomachinery, Vol. 114, pp. 27-37.
- [23] Zangeneh, M., 1993, "Inviscid/viscous interaction method for 3D inverse design of centrifugal impellers", ASME J. of Turbomachinery, Vol. 118, pp. 385-393. Also ASME paper No. 93- GT-103.
- [24] Japikse, D., 1987, "A Critical Evaluation of Three Centrifugal Compressors With Pedigree Data Sets: Part 5—Studies in Component Performance," Journal of Turbomachinery, January 1987, Vol. 109/1-9.
- [25] Li, H., Su X. R., and Yuan, X., 2019, "Entropy Analysis of the Flat Tip Leakage Flow with Delayed Detached Eddy Simulation," Entropy 2019, 21(1), 21.
- [26] Krain, H and Hofmann, B, 1998, 'Flow Physics in High Pressure Centrifugal Compressors', ASME FEDSM98-4853.
- [27] Eisenlohr, G., Krain, H., Richter, F. and Tiede, V. "Investigations of the Flow Through a High Pressure Ratio Centrifugal Impeller ." ASME GT-2002-30394, Jan 2002: 9.
- [28] TURBOdesign1, Version 6.8.0, 2019, Advanced Design Technology Ltd. London, UK.

- [29] TURBOdesign Suite, Version 6.8.0, 2019, Advanced Design Technology Ltd. London, UK.
- [30] Zangeneh, M., Amarel, N., Daneshkhah, K., Krain, H., 2011, "Optimization of 6.2:1 Pressure Ratio Centrifugal Compressor Impeller by 3D Inverse Design," Proceedings of ASME Turbo Expo 2011, June 6-10, 2011, Vancouver, British Columbia, Canada.